Reviews of Electromagnetics, Vol. IV, 2025
EuCAP 2025 Special Issue
DOI: 10.53792/RoE/2025/25008

Reviews of Electromagnetics
EuCAP 2025 Special Issue

3D-Printed Dual-Band and Broadband Linear to Circular Polarizing Screen for K/Ka-Band Satellite Antennas With Feed-Aperture Integration

Andrea Guarriello[1]*, Etienne Girard[1], Charalampos Stoumpos[2], Laszlo Sajti [3], Frederic Veron[1], Hervé Legay[1]

Abstract
This paper presents the design, fabrication, and experimental validation of a dual-band linear-to-circular polarization converter based on a 3D frequency selective surface and tailored for K/Ka-band satellite communication systems. The proposed solution, based on a transverse electromagnetic (TEM) cell topology, is realized through additive manufacturing using Stereolithography Apparatus (SLA) combined with copper metallization, achieving a lightweight and low-loss structure with complex 3D geometries. The device, integrated directly on the the feed aperture, effectively covers both the transmit K-band (17.3–20.2 GHz) and receive Ka-band (27.5–30.0 GHz) sub-bands, demonstrating axial ratios (AR) below 1.1 dB in the TX and in the RX band, with reflection losses better than 17 dB. The polarizing screen demonstrates outstanding broadband or dual-band behavior under periodic boundary condition simulations ($AR < 3$ dB and $IL < 0.25$ dB in broadband mode; $AR < 1.1$ dB and $IL < 0.15$ dB in dual-band mode). This work represents a first step toward the direct integration of polarizing screens onto radiating apertures, enabling compact, high-efficiency antenna designs for future phased array platforms. The paper also discusses fabrication challenges, thermal reliability, and a sensitivity analysis confirming robustness against manufacturing tolerances, highlighting the potential of 3D printing for advanced satellite antenna subsystems.

Key terms
Polarization conversion, 3D Frequency Selective Surfaces, Dual-Band Polarizer, Broadband Polarizer, 3D-Printing, Stereolithography.

[1] *Thales Alenia Space, Toulouse, France,*
[2] *IETR, INSA of Rennes, Rennes, France*
[3] *RHP-Technology GmbH, 2444 Seibersdorf, Austria*
*__Corresponding author__: Andrea.Guarriello@thalesaleniaspace.com

Received: 22/05/2025, Accepted: 14/06/2025, Published: 28/11/2025

1. Introduction

In the context of next-generation geostationary (GEO) telecommunications satellites that demand ultra-high-throughput communication systems, high-efficiency linearly polarized radiating elements have been successfully developed and validated [1, 2]. However, circular polarization remains essential to enhancing the robustness and performance of satellite communication links. It mitigates critical issues such as polarization mismatch, multipath propagation, and ionospheric depolarization effects, all of which can significantly degrade linearly polarized signals.

State-of-the-art dual-band, high-aperture-efficiency antenna feeds are typically based on profiled stepped or sloped horn antennas [3], where circular polarization is achieved using a septum polarizer. While this configuration provides aperture efficiencies of approximately 85% over 10% and 6% fractional bandwidths in the transmit and receive bands, respectively, it is not without challenges. These include the quasi-stochastic nature of the horn profile optimization, the substantial height of the feed (often on the order of $10\lambda_0$), and the complexity of designing a dual-polarized septum polarizer, especially in

the Rx band, where higher-order modes excitation is no longer negligible.

Alternative approaches have emerged in recent years. One promising direction involves the use of dual-band metamaterial-based short backfire antennas [4], which can achieve near-100% aperture efficiency. However, these systems are limited by the inherently dispersive behavior of anisotropic materials, as well as practical complexities such as intricate feeding networks, embedded dielectrics, and specialized circular polarization feeding mechanisms. Another advanced design involves ultra-wideband, dual-circularly polarized waveguide antenna arrays with corporate feeding networks that incorporate septum polarizers at each element input [5]. While these systems achieve over 80% aperture efficiency across a wide 45% bandwidth (from 19 to 30 GHz), they still fall short of simultaneously covering the full dual K-band (17.3–20.2 GHz for TX) and Ka-band (27.5–30.0 GHz for RX) ranges.

In this work, we pursue an alternative strategy that involves integrating a polarizing screen directly onto a novel, dual-band, high-aperture-efficiency radiating element. This approach enables compact and high-performance designs that are particularly beneficial for phased array architectures in spaceborne systems, where size, weight, and complexity are critical constraints. In such configurations, the ability to transform linearly polarized waves into circular polarization (and vice versa) at the aperture plane—without resorting to traditional in-line polarizing components—is a highly desirable feature.

Substantial progress has been made in recent years in the development of linear-to-circular polarization converters using frequency-selective surfaces (FSSs) and periodic structures. These elements manipulate the polarization state of electromagnetic waves using a variety of two-dimensional and three-dimensional metallic patterns, such as rectangular patches and slots [6], meander-line configurations [7, 8, 9, 10], split-ring resonators [11], cross and Jerusalem cross structures [12, 13], and I- or H-shaped patterns [14], often aiming for angular stability through miniaturization. While these designs offer effective performance over single or dual bands, their practical implementation is often limited by fabrication complexity and the use of lossy dielectric substrates.

Innovative fabrication techniques, including 3D-printed metallic structures [14, 15] and precision-machined metal screens [10, 13, 16], have emerged as viable paths toward low-loss, robust devices for harsh environments. Though full-metal designs eliminate dielectric losses, they increase component mass and can impose additional manufacturing constraints [15]. Many of these works have also demonstrated the usefulness of equivalent circuit models for efficient design synthesis and optimization [15, 17].

In this paper, we present the design, fabrication, and experimental characterization of a novel linear-to-circular polarization converter for dual-band K/Ka-band satellite applications, covering the TX (17.3–20.2 GHz) and RX (27.5–30.0 GHz) bands. The proposed design draws upon the circuit modeling approach of [15], but is re-optimized for operation under limited scan angles typical of GEO missions (i.e., $\theta^{\text{scan}} < 10^\circ$). The converter is specifically engineered for additive manufacturing using Stereolithography Apparatus (SLA), allowing the realization of fine 3D geometries with high dimensional accuracy and low weight. The use of thin copper metallization ensures high conductivity without significantly increasing mass, enabling a compact and electrically efficient design.

The paper is structured as follows: Section 2 introduces the polarization conversion principles driving the design objectives. Section 3 presents the equivalent circuit modeling and unit cell performance under periodic boundary conditions. Section 4 discusses the integration of the polarizer with an innovative high-efficiency dual-band radiating element. Section 5 details the fabrication process using SLA and subsequent copper metallization. Section 6 provides a unit cell sensitivity analysis to assess robustness against geometric deviations. Section 7 presents experimental measurements validating the proposed design. Finally, Section 8 concludes the paper and outlines future perspectives.

2. Polarization conversion principles

The basic operating principle of a polarization converter is schematically illustrated in Fig. 1. We consider an incident linearly polarized wave, represented by its electric field vector $\mathbf{E_i}$ aligned along a reference axis $\hat{x}$ (defined as vertically polarized). If this electric field is tilted in the plane normal to the propagation direction, it can be decomposed into $\hat{x}$ and $\hat{y}$ components (corresponding to vertical and horizontal polarizations, respectively). To convert the linearly polarized wave into a circularly polarized transmitted wave $\mathbf{E_t}$, two key conditions must be met: 1) the amplitudes of the transmitted components should be as balanced as possible, and their vector sum should closely match the incident field's amplitude to minimize losses, and 2) the phase difference between the two transmitted components must be $\pm 90^\circ$.

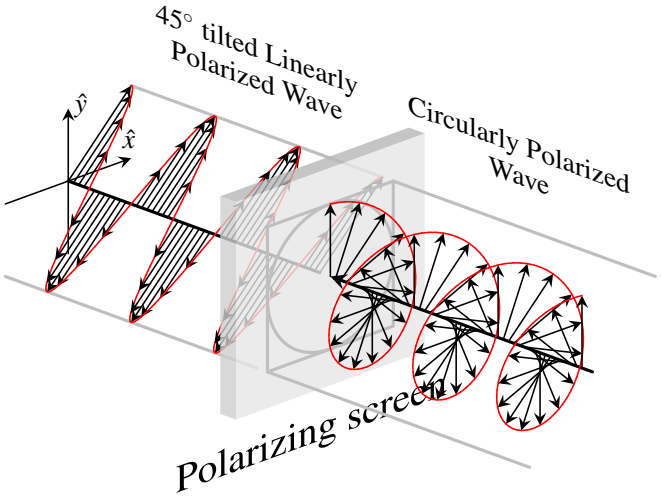

Figure 1: Schematic of polarizing screen operating principle.

The conditions can be expressed as follows:

$$\mathbf{E_i} = (E_i^x \hat{x} + E_i^y \hat{y}) e^{-jkz} \tag{1}$$

$$\mathbf{E_t} = (E_t^x e^{j\varphi^x} \hat{x} + E_t^y e^{j\varphi^y} \hat{y}) e^{-jkz} \tag{2}$$

These principles also apply to the reverse process of circular-to-linear polarization conversion. Ideally, the unit cell should act as a transparent screen, transmitting energy while manipulating the field components to meet the above mentioned conditions.

A critical metric for assessing the efficiency of linear-to-circular polarization conversion is the axial ratio (AR). The phase difference between the linear components is $\Delta\varphi = |\varphi^x - \varphi^y|$, and the axial ratio of the transmitted field is given by:

$$AR = \sqrt{\frac{|E_t^x|^2+|E_t^y|^2+\sqrt{\alpha}}{|E_t^x|^2+|E_t^y|^2-\sqrt{\alpha}}} \tag{3}$$

where $\alpha = |E_t^x|^4+|E_t^y|^4+2|E_t^x|^2|E_t^y|^2\cos 2\Delta\varphi$. A perfectly circularly polarized wave, characterized by orthogonal, balanced components and a phase difference of $\Delta\varphi = \pm 90°$, has an axial ratio of unity (0 dB). The axial ratio is also directly related to the cross-polarization discrimination (XPD) for circularly polarized waves:

$$XPD = \frac{1+AR}{1-AR} \tag{4}$$

3. Unit cell design and performances under periodic boundary conditions

The unit cell design is based on a transverse electromagnetic (TEM) topology, realized through a rectangular waveguide structure with four longitudinal slits on its lateral walls. This configuration, referred to hereafter as the "bare TEM cell," was initially introduced in [15] and has since been successfully adapted for multiple applications such as polarizing screens [15], dichroic mirrors [18], and impedance matching metasurfaces [19]. The bare TEM cell mimics the behavior of a parallel plate waveguide (PPW) with sub-wavelength periodicity and exhibits key advantages, including a wide operational bandwidth, the absence of a cut-off frequency, and robustness against variations in the angle of incidence. These characteristics render it particularly well-suited for additive manufacturing and advanced RF applications.

At its core, the bare TEM cell acts as a transmission line (TL) segment, where the physical length of the waveguide corresponds to the electrical length of the TL, and the characteristic impedance is governed by the longitudinal slit dimensions and periodicity (Fig. 2). Conceptually, this setup can be viewed as an air-filled dielectric slab under plane wave incidence, but with the added benefit of increased tunability. The slit dimensions in both x and y directions (w_x, w_y) enable decoupled control of impedance for orthogonal polarizations. Furthermore, by introducing stepped slits along the longitudinal direction, one can implement a multi-section TL model. This facilitates more refined input/output impedance matching and increases the available degrees of freedom in the design (see Fig. 2c and Fig. 2d).

The polarization-selective behavior of the structure is achieved through the inclusion of four cylindrical metallic bars placed within the waveguide. These elements behave either as inductive or capacitive loads, depending on the polarization of the incident wave. Analogous to printed strip gratings over dielectric layers, these bars provide a 3D realization of polarization control. For instance, the radius of the bars (r) and the spacing between them (A), depicted in Fig. 2b, directly influence the equivalent capacitance and inductance. Larger radii and greater spacing decrease inductance, whereas smaller radii and tighter spacing enhance capacitive coupling, thus enabling fine-tuned electromagnetic responses.

3.1. Equivalent circuit model

To gain deeper insight into the underlying mechanism and to enable systematic design, an equivalent circuit model is employed, as described in [15] and reoriented here for broadband dual-band operation in the K/Ka-band (TX/RX). The incident electric field, assumed to be slanted at $\pm 45°$ in the xy-plane, can be decomposed into two orthogonal components: the horizontal (E_x, H-pol) and vertical (E_y, V-pol) polarizations. Each polarization is modeled using an equivalent circuit: H-pol corresponds to Fig. 3a and V-pol to Fig. 3b.

The H-polarized model (Fig. 3a) is characterized by two cascaded transmission-line sections, described by impedance Z_1 and Z_2 and lengths d_1 and d_2, associated with the two longitudinally stepped slits ($w_{x,1}$ and $w_{x,2}$). A lumped capacitor C models the effect of the metallic bars for this polarization, with the spacing between bars denoted as d_{bars} and the total longitudinal length of the cell as d. In the V-pol configuration (Fig. 3b), the same structure is analyzed but with the orientation of the bars now vertical, effectively acting as a lumped inductance L rather than a capacitance.

The synthesis procedure of this equivalent circuit begins by characterizing the "unloaded" cell—i.e., the TEM structure without the metallic bar inclusions. In this configuration, the geometry translates to three cascaded transmission line sections: two identical segments with impedance Z_1 and length d_1, and a central segment with impedance Z_2 and length d_2. Geometrical parameters such as periodicities (p_x, p_y), wall thicknesses (t_x, t_y), and slit widths ($w_{x,1|2}$, $w_{y,1|2}$) are set as constants or sweep variables depending on the parameter under study. A lookup table is created to map the changes in circuit parameters to corresponding geometrical modifications.

The second step involves introducing a single pair of metallic bars into the structure. For E_x excitation, this translates to a capacitance (C), while for E_y excitation, it becomes an inductance (L). In both cases, the radius (r) and the separation (A) of the bars govern these equivalent circuit values, and corresponding lookup tables are created for each scenario. Finally, a second pair of bars identical to the first is added, separated by a distance d_{bars}, which maps directly to the final circuit length d_3.

Due to mutual coupling among the unit cell components (walls, slits, periodicity, and bars) fine-tuning was essential to ensure accurate curve-fitting between full-wave and equivalent circuit models. This adjustment step was particularly critical to maintain a high correlation with full-wave simulation results.

Using the established lookup tables, a two-step optimization strategy is employed. First, the V-pol bandpass response is synthesized by adjusting the parameters in Fig. 3b: Z_1, Z_2, d_1, d_2, d_3, and L. Once this is achieved, the H-pol response (Fig. 3a) is optimized by tuning the same structural parameters with C substituted for L. In this stage, both transmission losses and phase alignment, specifically achieving a $\pm 90°$ phase shift

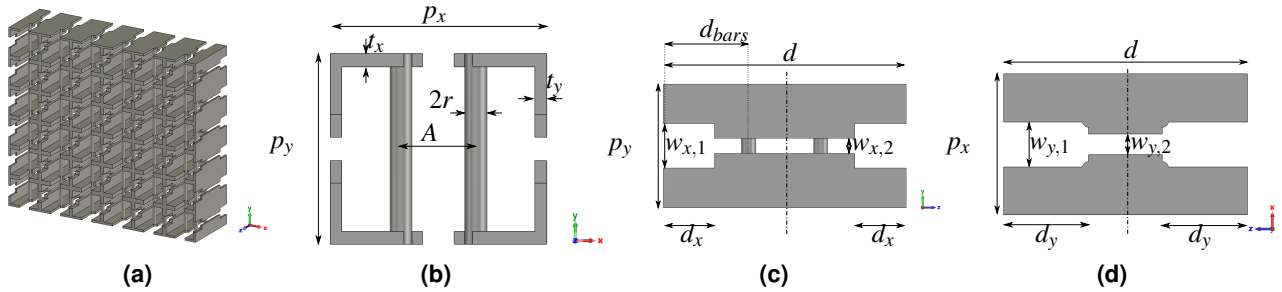

Figure 2: Unit cell topology and relevant geometrical parameters. (a) unit cell in periodic environment view, (b) top view, (c) side view, yz plane view, (c) side view, xz plane view.

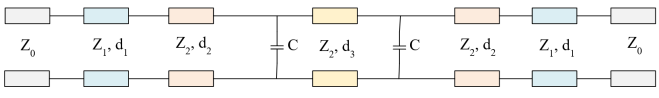

(a) The equivalent circuit for H-pol (E_x incidence) associated with the unit cell in Fig. 2.

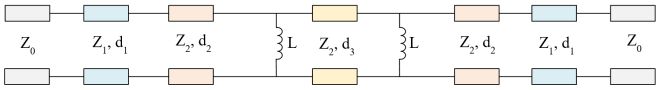

(b) The equivalent circuit for V-pol (E_y incidence) associated with the unit cell in Fig. 2.

Figure 3: Equivalent circuit model for the two polarizations

between the two polarizations, are carefully considered. Final circuit parameter values are annotated below Fig. 3a and Fig. 3b.

The comparison between full-wave simulations and equivalent circuit results is presented in Fig. 4, Fig. 5, where the magnitude and phase of the scattering parameters are plotted versus frequency for both polarization states. The agreement between the two models is notably high, with only minor deviations at higher frequencies. These discrepancies are attributed to the simplified nature of the equivalent circuit, which omits higher-order modal interactions, and to the proximity of the unit cell periodicity to half a wavelength at 30 GHz ($p_x \approx 0.54\lambda$, $p_y \approx 0.475\lambda$), thereby approaching the onset of higher-order Floquet modes. This phenomenon was previously discussed in [18], where better conformity was observed for smaller periodicity, typically below $0.4\lambda_{high}$.

The agreement is particularly strong for the V-pol case, which can be rationalized by two factors. Firstly, the smaller periodicity along the y-direction ($p_y < p_x$) enhances the quasi-static behavior and suppresses higher-order modes. Secondly, inductive elements in the equivalent circuit are generally more robust in capturing broadband characteristics than capacitive ones, as already noted in [15]. Fig. 5b further confirms this by showing the phase difference between the H-pol and V-pol transmission coefficients from both models, highlighting excellent agreement up to 30 GHz, after which small divergences begin to appear.

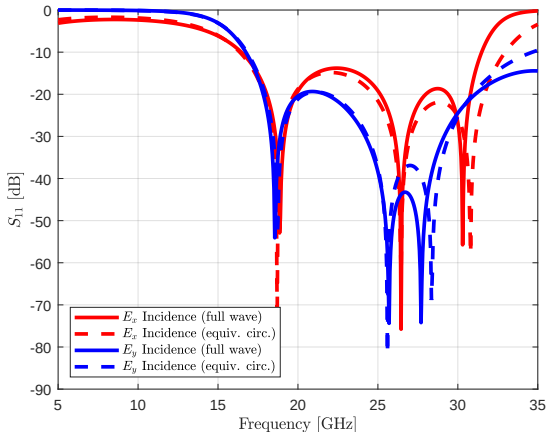

(a) Amplitude of the reflection coefficient computed through full wave simulation (continuous line), and the equivalent circuit model approach (dashed line).

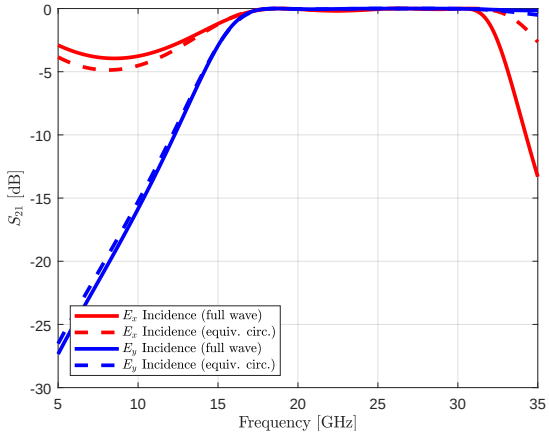

(b) Amplitude of the transmission coefficient computed through full wave simulation (continuous line), and the equivalent circuit model approach (dashed line).

Figure 4: Comparison equivalent circuit model vs full wave simulation for the amplitude of reflection and transmission coefficients. The EC model values, with reference to Fig. 3 are for H-pol: $Z_0 = 377\Omega$, $Z_1 = 196\Omega$, $Z_2 = 125\Omega$, $d_1 = 3.46$ mm, $d_2 = 0.02$ mm, $d_3 = 2.6$ mm, $C = 45$ fF. For V-pol: $Z_0 = 377\Omega$, $Z_1 = 228\Omega$, $Z_2 = 110\Omega$, $d_1 = 2.20$ mm, $d_2 = 1$ mm, $d_3 = 3.12$ mm, $L = 0.86$ nH.

3.2. Final unit cell performances

The design achieves low insertion losses by carefully tuning the slit geometry and waveguide length. A two-step slit configura-

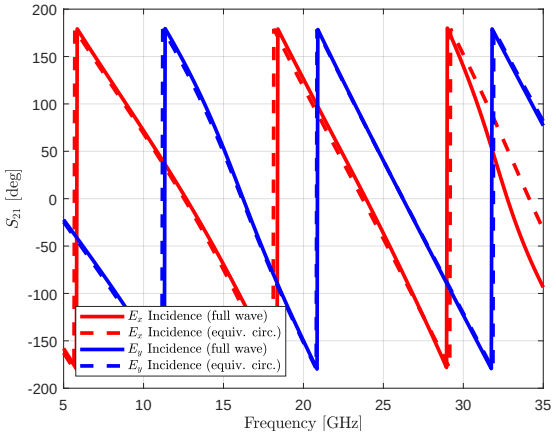

(a) Phase of the transmission coefficient computed through full wave simulation (continuous line), and the equivalent circuit model approach (dashed line).

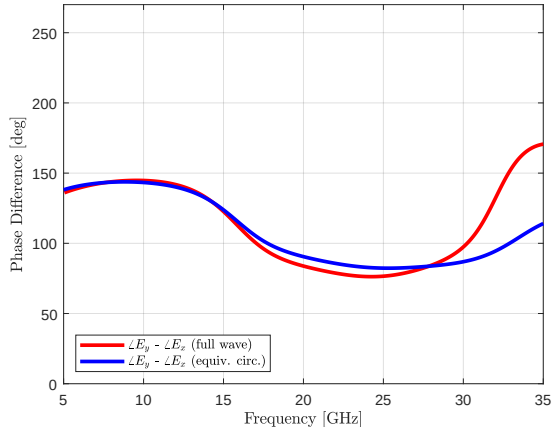

(b) Phase difference between the components of the transmission coefficient computed through full wave simulation (continuous line), and the equivalent circuit model approach (dashed line).

Figure 5: Comparison equivalent circuit model vs full wave simulation for the phase of transmission coefficients. The EC model values, with reference to Fig. 3 are for H-pol: $Z_0 = 377\Omega$, $Z_1 = 196\Omega$, $Z_2 = 125\Omega$, $d_1 = 3.46$ mm, $d_2 = 0.02$ mm, $d_3 = 2.6$ mm, $C = 45$ fF. For V-pol: $Z_0 = 377\Omega$, $Z_1 = 228\Omega$, $Z_2 = 110\Omega$, $d_1 = 2.20$ mm, $d_2 = 1$ mm, $d_3 = 3.12$ mm, $L = 0.86$ nH.

tion is employed on all orthogonal faces, and key geometric parameters (d, $d_{x|y}$, $w_{x,1|2}$, $w_{y,1|2}$) are optimized through full-wave simulation under periodic boundary conditions. The structure supports dual-band K/Ka-band operation with axial ratios below 1.1 dB, insertion losses under 0.15 dB, and return losses better than –15 dB for angles up to 10°, satisfying GEO mission standards. The overall performance is visualized in Fig. 6, where a broad axial ratio bandwidth (AR < 3) and fractional bandwidth of 57.3% (from 17.3 to 31.2 GHz) are demonstrated—making it one of the most efficient wide-band polarizing metasurfaces in the literature.

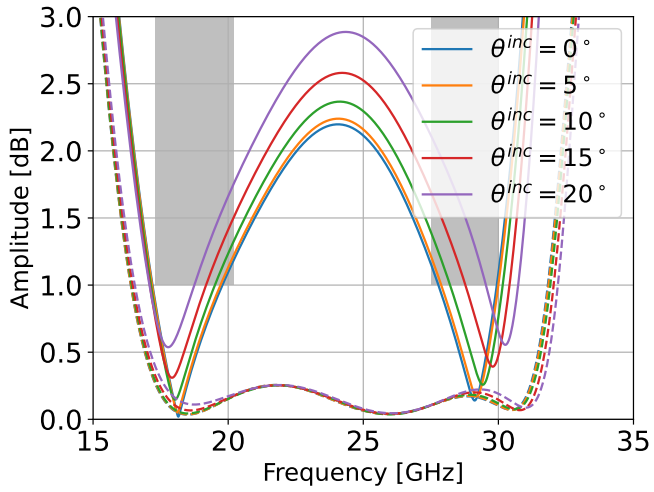

(a)

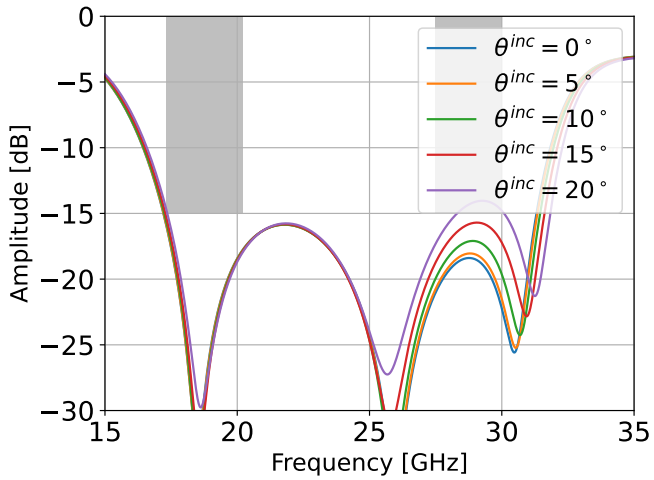

(b)

Figure 6: Performance of the unit cell with periodic boundary conditions under plane wave incidence at angle θ^{inc}. Relevant geometric parameters (in mm) are: $p_x = 5.4$, $p_y = 4.75$, $d = 9.35$, $t_x = 0.29$, $t_y = 0.32$, $w_{x,1} = 1.71$, $w_{x,2} = 0.58$, $w_{y,1} = 1.72$, $w_{y,2} = 0.79$, $d_x = 1.97$, $d_y = 1.71$, $r = 0.28$, $A = 1.87$, and $d_{bars} = 1.71$. (a) Axial ratio (solid lines) and insertion plus conductivity transmission losses (dashed lines), with gray areas indicating target specifications ($AR < 1$ dB in Ka-TX and Ka-RX bands). (b) Reflection coefficient, with gray areas showing target specifications ($S_{11} < -15$ dB in Ka-TX and Ka-RX bands).

4. Coupling the polarizer with a high efficiency dual band radiating element

4.1. Compact high efficiency radiating element for dual band shared aperture phased array

As part of the ESA-supported ACTA-UHTS project [1], the team extended its prior work on the Quad-Furcated Profiled Horn (Q-FPH) design [20] to meet the stringent requirements of K/Ka-band high-efficiency feeds, both in terms of performance and manufacturability.

The foundation of this development lies in the growing demand for high-speed broadband satellite connectivity, addressed by geostationary Very High Throughput Satellite (VHTS) systems. Currently, the Eutelsat Konnect VHTS satellite delivers up to 500 Gbit/s through multi-beam coverage and aggressive frequency reuse. However, future systems aim to achieve Ultra High Throughput Satellite (UHTS) performance, with aggregate throughput exceeding 1 Tb/s. This leap in capacity requires larger apertures and a greater number of narrowly focused beams.

In this context, Direct Radiating Arrays (DRAs) present a more scalable and flexible solution than conventional passive multi-beam antennas. DRAs enable distributed amplification and beam-forming flexibility, allowing capacity to be dynamically steered across the visible Earth. To reduce system complexity and cost, especially in the Beam Forming Network (BFN), it becomes crucial to minimize the number of RF chains and ports. This motivates the use of large-aperture radiating elements, which enable sparse array configurations without introducing grating lobes, provided that the inter-element spacing remains below the critical threshold for scan angles up to $\pm 8.7°$, as required for GEO coverage. The phased array should work simultaneously in Tx and Rx bands, implying a shared aperture, as shown in Fig. 7.

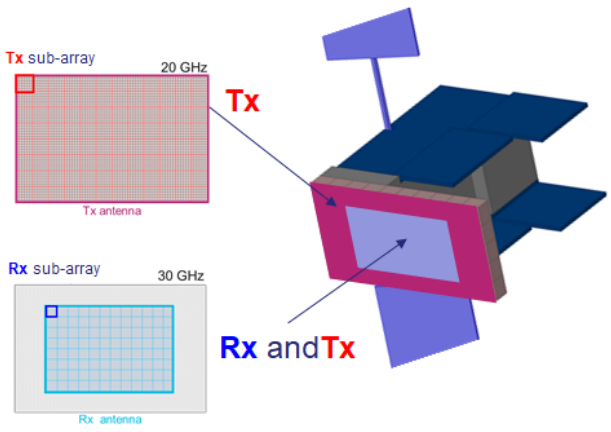

Figure 7: ACTA-UHTS single antenna operating simultaneously in Ka-Tx and Ka-Rx bands.

To address these constraints, the ACTA-UHTS feed design employs an innovative shared-aperture concept. The radiating element consists of a multi-port configuration: four independent smaller apertures operate in the Ka-Rx band, each fed individually, while the Ka-Tx band uses a combined excitation through a fixed power combiner, effectively transforming the four sub-apertures into a single radiating element (Fig. 8).

This dual-band architecture is optimized for high aperture efficiency in both Tx and Rx. The design controls the modal content within the horn by shaping the horn profile to manipulate the excitation of TE_{10}, TE_{30}, and TE_{50} modes. The result is a near-uniform electric field distribution across the aperture, essential for achieving high surface efficiency (Fig. 9a and Fig. 9b).

Figure 8: Concept of the shared-aperture radiating element with independent Rx and combined Tx paths.

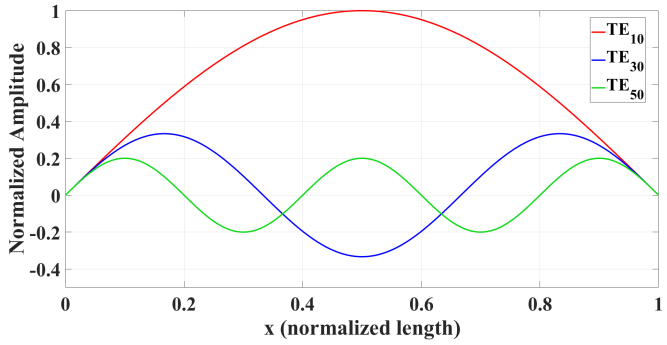

(a) Mode shaping in the shared aperture.

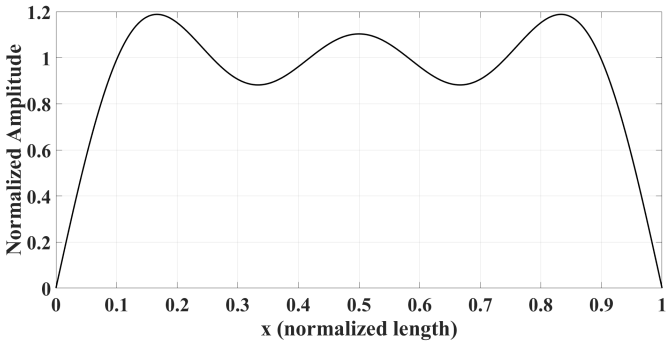

(b) Uniform field distribution at aperture for high efficiency.

Figure 9: Field shaping in the Q-FPH shared aperture feed.

The horn profile directly governs modal propagation, but only for polarizations aligned with the corresponding wall. Thus, the X-aligned horn profile controls Rx performance (vertical polarization), and the Y-aligned profile shapes Tx behavior (horizontal polarization), enabling decoupled design and optimization for each sub-band (Fig. 10).

The feed is manufactured using 3D-printing technologies [2], resulting in a lightweight component (81 g excluding flanges), with a thin 1 mm wall and a length-to-height ratio of 2.5. Measured aperture efficiencies are excellent: 85–90% in Ka-Tx and 75–80% in Ka-Rx. The system operates in horizontal polarization for Tx and vertical for Rx (Fig. 11).

To transform the dual linear polarization into circular polarization, various options were assessed. While waveguide septum polarizers or dual-band iris polarizers are commonly used in such applications, they were ultimately deemed unsuitable for this design for both practical and fundamental reasons.

First, placing these polarizers at the excitation port level

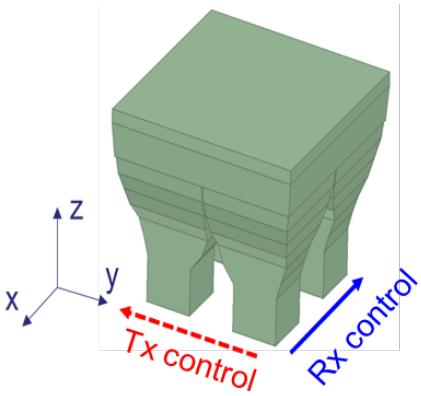

Figure 10: Independent X and Y horn profiles enable dual-band performance.

Figure 11: 3D-printed feed showcasing the Q-FPH design.

introduces a substantial bulk, increasing the axial length of the feed and complicating integration. In contrast, the thin polarizing screen positioned at the feed aperture provides a much more compact solution.

Second, and more critically, traditional septum or iris polarizers require symmetrical horn structures, typically with identical profiles along both the x and y directions, to ensure proper mode coupling and polarization transformation. The Q-FPH design, however, intentionally features asymmetric profiles in x and y to independently control the modal content and radiation pattern for Tx and Rx bands. This breaks the symmetry needed for proper septum or iris polarizer operation and makes their integration incompatible with the desired dual-band, dual-linear, and decoupled design.

In summary, the aperture-mounted polarizing screen not only offers superior compactness but is also the only viable solution compatible with the Q-FPH architecture, preserving the independent design pathways for the Tx and Rx bands while achieving high polarization purity and efficiency.

4.2. Installing the polarizing screen directly on the radiating element aperture

The polarizing screen is mounted at a 45° tilt with respect to the feed aperture plane, as discussed in Section 3. This orientation facilitates the conversion of horizontal polarization into right-hand circular polarization (RHCP) and vertical polarization into left-hand circular polarization (LHCP). Ideally, the polarizing structure would be directly integrated onto the radiating aperture via monolithic 3D printing. The present study represents a first step toward such integration of polarizing or multifunctional screens with radiating apertures, enabling compact and efficient antenna architectures.

Fig. 12 illustrates the CAD model of the radiating element equipped with the feed and polarizing screen. In this work, the polarizer is optimized independently of its electromagnetic coupling to the feed, with the primary focus placed on minimizing return loss and achieving a low axial ratio. Although some interaction between the feed and screen is present, its impact on performance is limited (simulation and measurement results are presented in Section 7).

A parametric study was conducted to determine the optimal offset distance h between the polarizing screen and the feed flanges. The goal was to minimize transmission losses and maintain high efficiency. The following figures of merit were evaluated across the TX and RX bands: the average broadside losses $|L_{bs}^{\mathrm{TX,RX}}|$ (to be minimized), the maximum losses $L_{\max}^{\mathrm{TX,RX}}$ over the angular range (to be minimized), the maximum axial ratio at broadside $AR_{\max}^{\mathrm{TX,RX}}$ (to be minimized), the maximum return loss across each band $RL_{\max}^{\mathrm{TX,RX}}$ (to be minimized), the average efficiency difference $|\Delta e^{\mathrm{TX,RX}}|$ computed as the linear difference between the feed-alone and feed-plus-polarizer configurations (to be minimized).

The results of this parametric analysis are summarized in Table 1, which serves as a decision matrix for selecting the optimal screen offset. The study confirms that while the offset does influence several key metrics, its overall effect is limited, demonstrating the robustness of the design. The optimal configuration was found for $h = 3.5$ mm, although performance at $h = 0$ mm was comparably acceptable. A detailed comparison of simulated and measured performance for both the feed and feed-plus-polarizer system is provided in Section 7.

5. Realization of the Metalized 3D Printed Screen through Stereolithography Apparatus (SLA)

5.1. Fabrication and Metallization Approach

For this breadboard prototype, stereolithography-compatible resins were selected to meet the thermal and mechanical requirements. The chosen material, Flame Retardant HDT by Liqcreate, provides mechanical rigidity and thermal stability above 200°C. This material enabled the realization of the intricate unit cell geometries required for dual-band polarization control, albeit near the spatial resolution limits of the printing process. Following the manufacturer's guidelines, the printed parts were post-cured under UV light at a temperature of 60°C

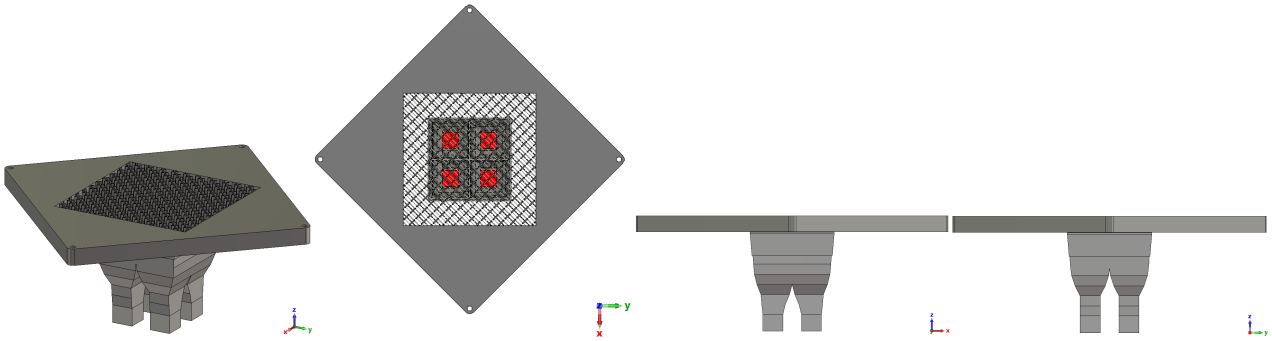

(a) Perspective view **(b)** Top view **(c)** Side view (XZ plane) **(d)** Side view (YZ plane)

Figure 12: Integration of the polarizing screen with the radiating element.

Table 1: Performance figures for varying polarizer screen distance h from the feed flanges.

Band	Figure of Merit	h=0 mm	h=1.75 mm	h=3.5 mm	h=5.25 mm	h=7 mm
TX	$\lvert L_{bs}^{TX}\rvert$ [dB]	0.3060	0.1203	0.1189	0.2169	0.3320
	L_{max}^{TX} [dB]	0.8569	0.4515	0.2011	0.3647	0.5552
	AR_{max}^{TX} [dB]	1.4709	0.8823	0.7458	1.0510	1.6880
	RL_{max}^{TX} [dB]	-16.2922	-18.7419	-18.3129	-15.3564	-14.3539
	$\lvert\Delta e^{TX}\rvert$	0.0399	0.0249	0.0348	0.0532	0.0481
RX	$\lvert L_{bs}^{RX}\rvert$ [dB]	-0.0078	0.0030	0.0350	0.0469	0.0161
	L_{max}^{RX} [dB]	0.0536	0.0959	0.1129	0.0804	0.1170
	AR_{max}^{RX} [dB]	2.0555	1.9451	2.1374	2.2253	2.0143
	RL_{max}^{RX} [dB]	-17.4843	-20.0564	-20.7464	-19.2998	-21.6572
	$\lvert\Delta e^{RX}\rvert$	0.0283	0.0153	0.0102	0.0252	0.0153

for 120 minutes (Fig. 13a). The printing was carried out using an advanced SLA printer at RHP Technology facilities. Fig. 13b shows the printed screen with a soluble wax support structure, which was employed to ensure an optimal printing orientation.

After the post-curing, the part was placed in a Petri dish with the water-soluble wax to facilitate support removal. Once the wax had fully hardened, the part was carefully removed from the Petri dish, and the support structure was removed by grinding. The printed parts were then immersed in a container with warm water placed on a magnetic stirrer until the wax dissolved completely. Finally, the parts were degreased using isopropanol.

Following the 3D printing and removal of the support structures, the polarizing screen was spray-coated with a conductive primer. This was followed by copper electrodeposition in an electrolyte bath, with an electric field applied between the anode and the workpiece (acting as the cathode), forcing charged metal ions to deposit as a metallic layer. A voltage of 1 V and a current of 500 mA were applied between the counter-electrode and the substrate (also known as the working electrode). The metal cations migrated to the working electrode, where they were reduced to oxidation state 0 and deposited as a metallic layer. The deposition process lasted 10 minutes (Fig. 14).

The component was then mounted (using adhesive) within a 3D-printed polymeric frame (made of VeroWhite material) to facilitate characterization without affecting the active metasurface (Fig. 15a). The electrochemical copper deposition

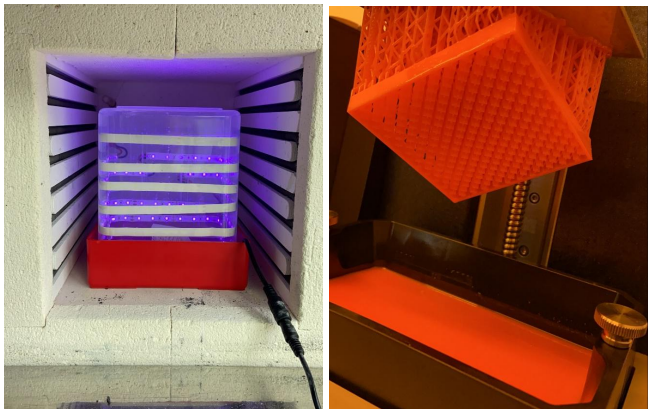

(a) **(b)**

Figure 13: UV curing process (a), manufactured screen with wax-soluble support (b).

produced continuous, pore-free copper layers (approximately 24 µm thick), with excellent adhesion, as confirmed by pull-off tests post-thermal cycling. The copper coating exhibited low electrical resistance ($8.3 \pm 1.1\,\mathrm{m\Omega}$) and RF-compatible surface quality with minimal roughness.

5.2. Thermal and Mechanical Inspection

The polarizing screen underwent thermal cycling, with 3×25 cycles performed at a rate of 8 K/min and a temperature range

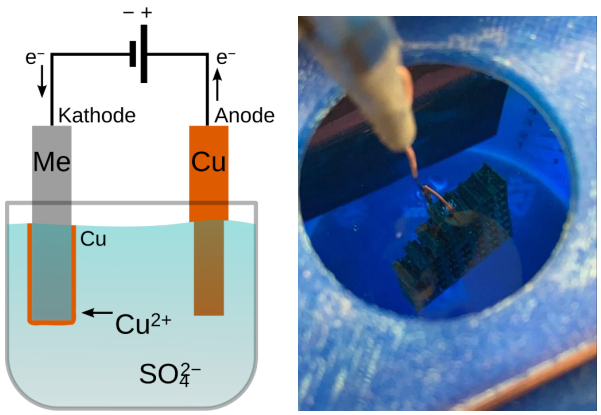

Figure 14: Copper coating through the galvanic process.

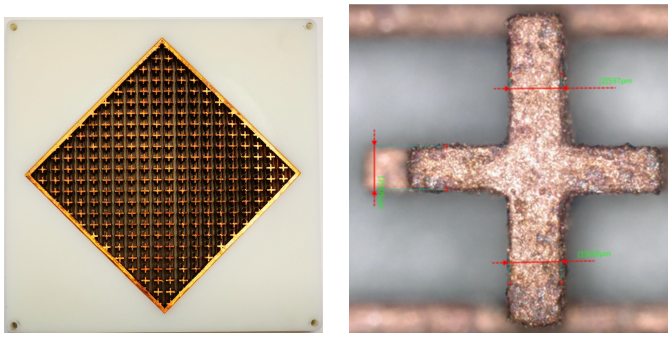

Figure 15: (a) Polarizing screen realized through SLA plus surface metallization (Cu) and mounted on a non-functional support (in white); (b) optical microscope visual inspection and measurement of some manufactured geometrical parameters.

of $\pm 100^{\circ}$C. Post-cycle inspections revealed no visible deformation, chipping, or delamination. No changes in electrical conductivity were observed, and the morphology of the metallization layer remained stable, as confirmed by SEM and cross-sectional analysis. The adhesion and electrical properties were comparable to untreated samples.

Optical microscope inspection was conducted to assess the dimensional compliance of the demonstrator with the nominal values. Deviations in the order of $30-40$ µm were observed, as shown in Fig. 15b. Table 2 summarizes the averaged measured geometrical parameters, the standard deviation, and the nominal values.

Table 2: Nominal and Measured Geometrical Parameters.

Parameter	Nominal (µm)	Avg. Measured (µm)	Std Dev. (µm)
$2 \times t_x$	580	591	66.1
$2 \times r$	580	588	159
$w_{y,2}$	780	792	70.7
$w_{x,2}$	590	583	40.5

6. Unit Cell Sensitivity Analysis

A unit-cell sensitivity analysis was conducted to assess the impact of manufacturing uncertainties on geometric parameters, with a deviation of ±50 µm applied to each parameter. This deviation was considered as a preliminary indication, whose magnitude was later confirmed through the visual inspection presented in Table 2. Given the complexity of the design (with at least 12 varying degrees of freedom), an exhaustive analysis would require 2^{12} simulations. Instead, a Monte Carlo simulation with 100 random cases was performed to simulate manufacturing uncertainties. Fig. 16a shows the nominal design (black line) for axial ratio and transmission losses, with random variations (red for axial ratio and orange for transmission losses). Fig. 16b shows the nominal reflection coefficient in black, with random cases in red. The analysis, conducted under periodic boundary conditions with normal incidence, demonstrated the robustness of the design, particularly regarding the reflection coefficient and transmission losses. The axial ratio remained below 3 dB even in extreme cases.

7. Measurement results

The measurement campaign on the feed alone and the feed plus polarizing screen assembly (Fig. 17) focused on return loss and directivity in the far field.

Return loss was measured across the entire K/Ka-band (17–30.5 GHz) at 100 MHz intervals, while radiation patterns were sampled 36 times per band: 17–20.5 GHz (TX) and 27–30.5 GHz (RX). The feed was excited as described in Section IV, with a single port used for TX and the four RX ports excited individually, then combined during post-processing. Simulations were configured accordingly for comparison. Fig. 18a and 18b show return loss measurements for both bands, comparing measurements of feed alone and feed plus polarizer with feed plus polarizer simulations. The polarizer's impact on return loss is minimal, with adaptation better than -17 dB across both bands. A slight mismatch appears between 17.3 GHz and 17.5 GHz, which is also present in the feed alone, indicating the polarizer is not the cause. However, adaptation better than -20 dB is achieved from 18.1–20.5 GHz, and -17 dB is maintained across the RX band, with good alignment between theory and experiment.

Fig. 19a and 19b compare simulations and measurements of the feed plus polarizer at center frequencies. Co-polarization profiles show excellent correlation, while cross-polarization shows good agreement at 28.7 GHz (RX), though a discrepancy exists at 18.7 GHz (TX). The polarizer does not alter the radiation pattern envelope, only the polarization status. Performance across the frequency range is summarized in Fig. 20a and 20b, showing broadside directivity of both the feed and feed plus polarizer. The polarizer efficiently converts H-pol into RHCP and V-pol into LHCP, with ripples of less than 0.4 dB and 0.2 dB, respectively, showing strong correlation with theoretical predictions.

Fig. 21a and 21b highlight the screen's cross-polarization discrimination (XPD). Simulations show XPD exceeding 25 dB (equivalent to $AR < 0.97$ dB) across the TX band, and 18 dB ($AR < 2.2$ dB) in the RX band. Measurements and simula-

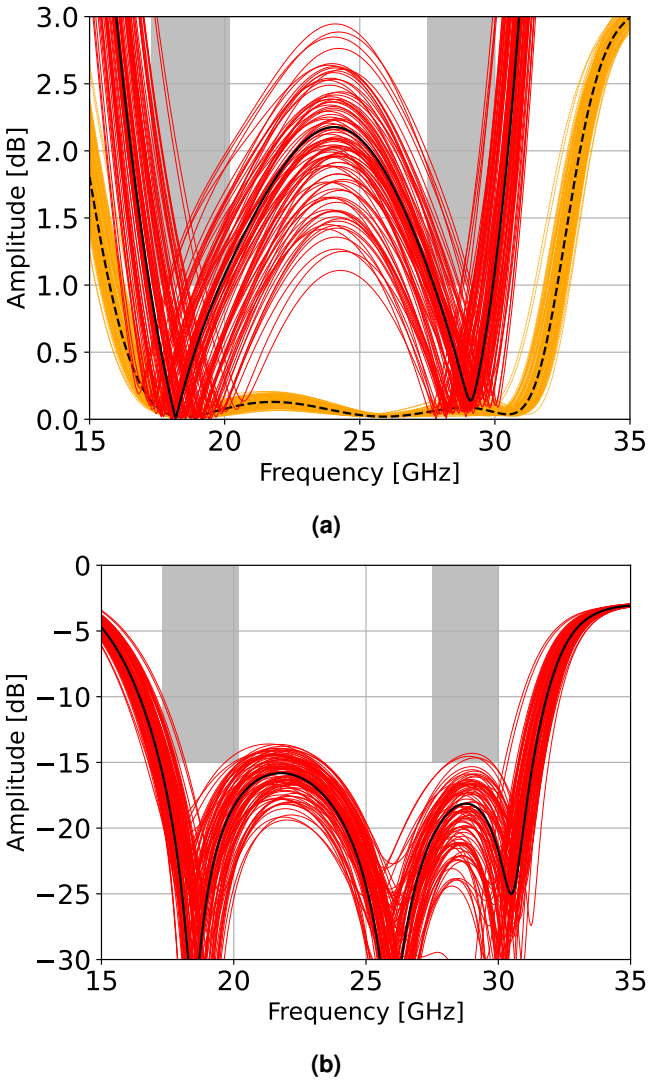

Figure 16: Monte Carlo sensitivity analysis results. (a) axial ratio (continuous black line), nominal design; red lines, altered geometrical parameters; dashed black line, nominal design for insertion and conductivity losses; dashed orange lines, altered geometrical parameters. (b) reflection coefficient, black line nominal design, red lines altered geometrical parameters.

tions correlate well in the RX band but show a drop in the TX band, likely due to manufacturing defects on the lateral slits regions affecting phase balance at lower frequencies. Despite this, the RX band results demonstrate the high quality of the manufacturing process, particularly in resolving fine details and metallization. Simulations indicate very low conductivity losses ($< 0.05dB$) for the copper metallization, though these couldn't be quantified with the current setup due to measurement limitations. Future work will assess this figure of merit using a high-precision quasi-optical bench, as done in previous works [15].

Table 3 below compares the performance of the proposed polarizing screen with state-of-the-art designs, emphasizing its impressive dual-band or broadband capabilities.

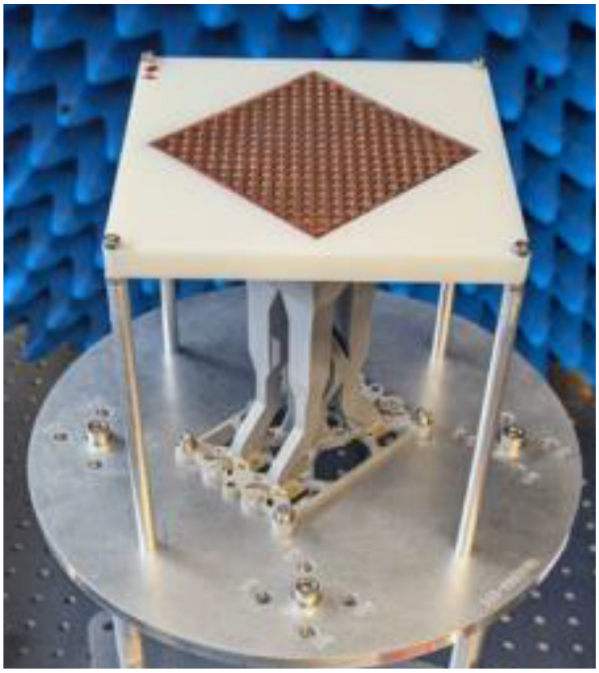

Figure 17: Polarizing screen realized through SLA plus surface metallization (Cu) and mounted on a non functional support (in white) and installed mounted on the 3D printed feed for the measurement setup.

8. Conclusions and Perspectives

This work presented the design, manufacturing, and testing of a linear-to-circular polarization converter specifically tailored for dual-band K/Ka-band satellite applications. The proposed approach, which combines advanced Stereolithography Apparatus (SLA) technology with a well-optimized transverse electromagnetic (TEM) cell structure, has resulted in a lightweight, low-loss design that outperforms existing solutions in terms of both efficiency and broadband capabilities. The integration of the polarizing screen directly onto the radiating element aperture represents a significant step toward more compact and high-performance radiating elements for phased array applications. By eliminating the need for separate polarizers and integrating the polarization control directly onto the feed aperture via monolithic 3D printing, the system can be significantly miniaturized without compromising performance.

When the polarizing screen is combined with a high-efficiency radiating element, simulation results demonstrate impressive performance, including an axial ratio below 1 dB for most of the TX band, below 2.2 dB for the RX band, and reflection losses of less than -17 dB in both operational bands. These results showcase the converter's suitability for modern satellite communication challenges. Experimental measurements confirm excellent agreement with simulations for the higher RX band and fair agreement for the lower TX band.

The simulation of the standalone polarizing screen (with periodic boundary conditions) shows outstanding performance in both dual-band mode (AR$<$ 1.1 dB, insertion losses $<$ 0.15 dB) and broadband mode (AR$<$ 3 dB, insertion losses$<$ 0.25 dB), highlighting the potential of this approach for high-efficiency

Table 3: Comparison with the state of the art linear to circular polarization converters screens.

Ref.	IL (dB)	AR (dB)	Dual BW (%)	IL (dB)	AR (dB)	Broad BW (%)	Technology	Angular stability (deg)
[8]	0.6	3	21.8/12.6	-	-	-	Single layer PCB	$0^\circ - 45^\circ$
[9]	-	-	-	1	2.5	57	Multilayer PCB	$0^\circ - 20^\circ$
[12]	2	3	29/12	-	-	-	Multilayer PCB	$0^\circ - 20^\circ$
[13]	0.7	1.7	2.5/1.7	-	-	-	Full metal	0°
[14]	1	3	3.5/3.2	-	-	-	Full metal	$0^\circ - 20^\circ$
[15]	-	-	-	0.5	3	37.8	Full metal	$0^\circ - 30^\circ$
[10]	-	-	-	1.65	3	25.45	Full metal	0°
[16]	0.8	3	12/12	-	-	-	Full metal	$0^\circ - 10^\circ$
This work	0.15	1.1	15.5/8.7	0.25	3	57.3	Full metal	$0^\circ - 20^\circ$

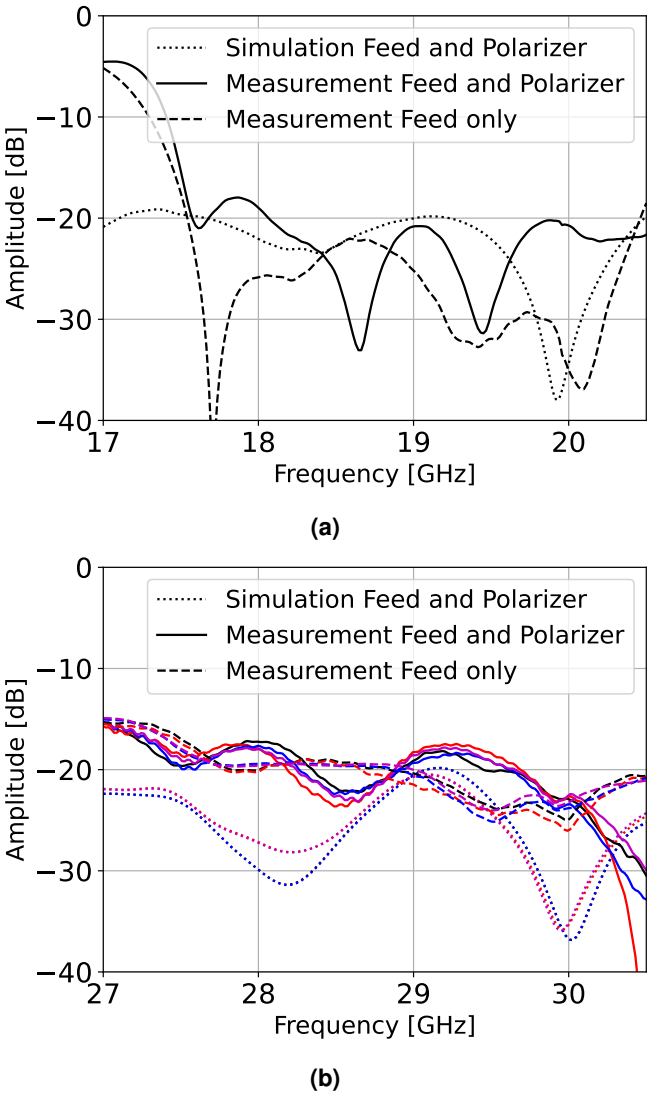

Figure 18: Return loss measurement (reflection parameter S_{ii}, where i is the port number) of the feed plus polarizer assembly (continuous line), feed alone (dashed line) and simulation results of the feed plus polarizer assembly (dotted line). (a) Ka-TX band, (b) Ka-RX band.

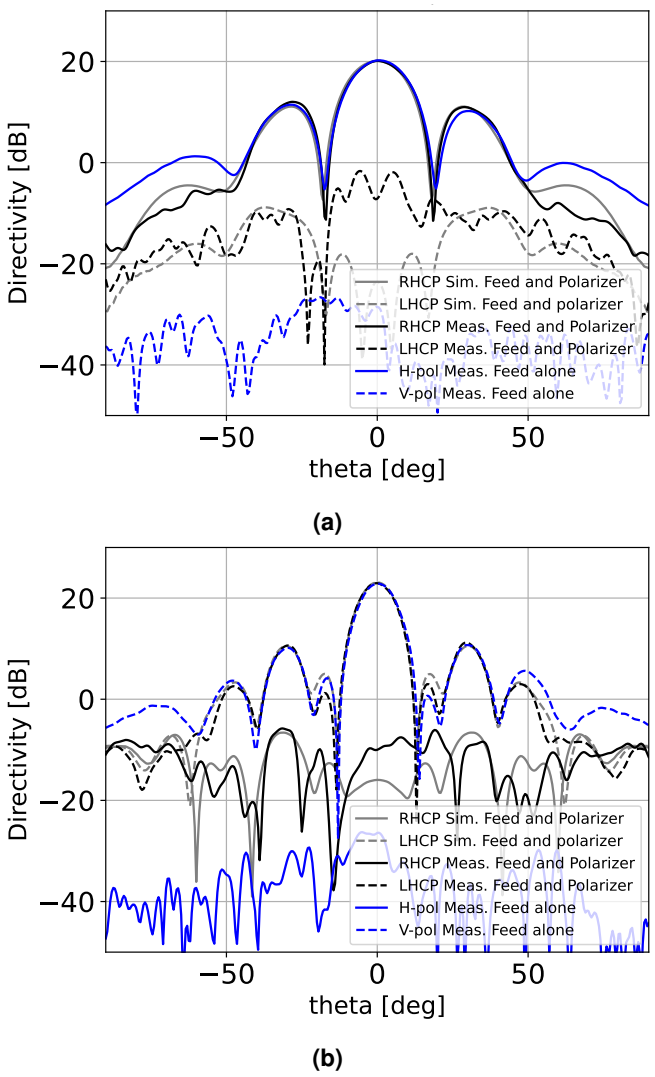

Figure 19: Measurements and simulations results: (a) radiation pattern at central frequency 18.7 GHz (a) and 28.7 GHz (b) for TX and RX bands respectively. Cut $\phi = 0$.

circularly polarized radiating elements. This work marks a significant leap in the design and manufacturing of high-performance frequency- and polarization-selective surfaces using advanced

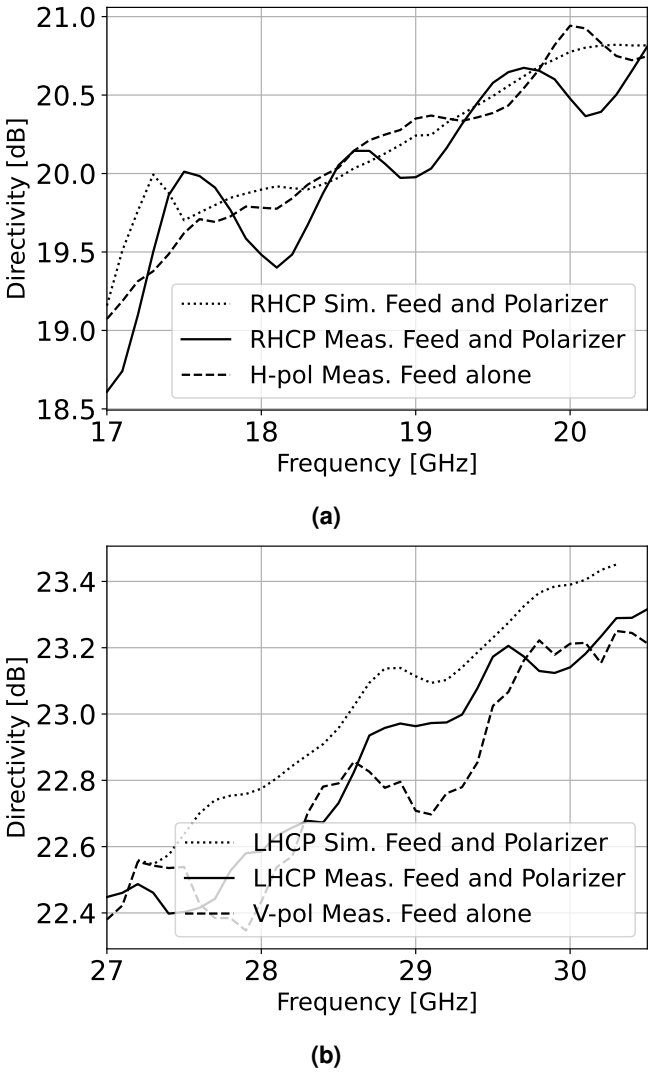

Figure 20: Measurements and simulations results: feed alone and feed plus polarizer broadside directivity over the TX (a) and RX (b) bands

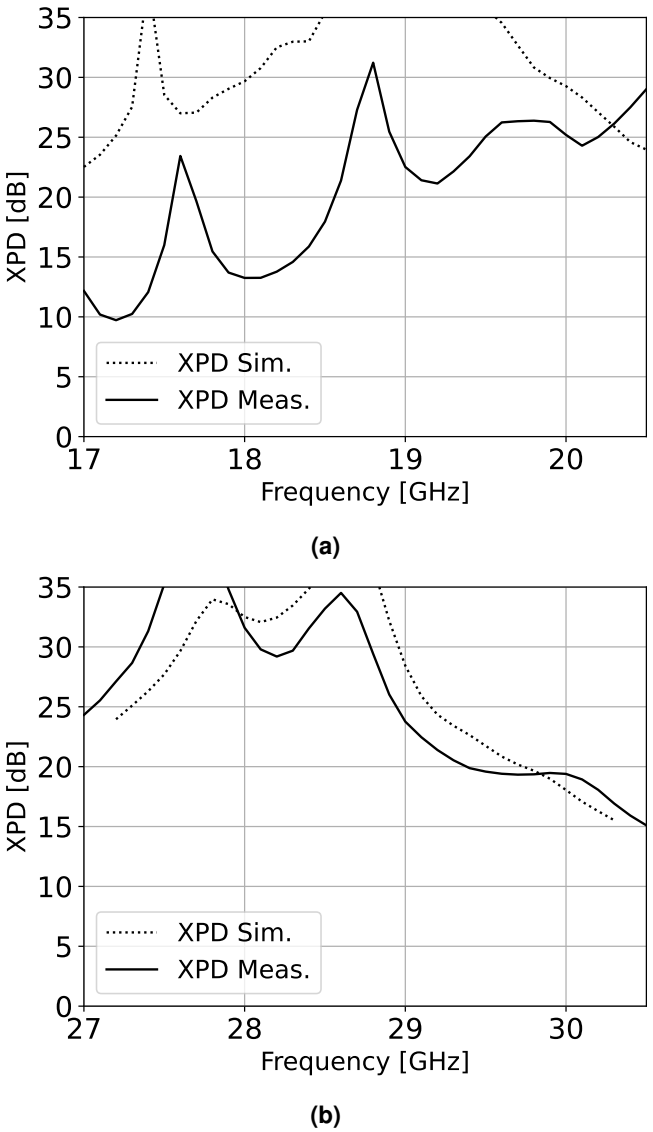

Figure 21: Measurements and simulations results: broadside XPD over the TX (e) and RX (f) bands.

3D printing techniques.

Looking forward, there are opportunities for further enhancing the figures of merit, particularly in areas where measurement discrepancies were observed. For example, improvements in the cross-polarization discrimination (XPD) and the axial ratio for the TX band would help achieve better overall performance in the lower frequency range. Additionally, the direct integration of the polarizing screen on the radiating element aperture, achieved through monolithic 3D printing, can be further refined by uniforming 3D printing techniques. As noted in this work, the radiating element was printed using Selective Laser Melting (SLM) technology, while the polarizing screen was fabricated using SLA. Future work will focus on the standardization of 3D printing techniques to ensure uniformity in material properties and to optimize the manufacturing process for large-scale production. The next step will also explore the integration of higher-order functionalities.

Acknowledgment

The authors would like to thank the European Space Agency (ESA) for funding the SELMET project, under which the polarization converter demonstrator was manufactured. They are also grateful to Maarten van der Vorst for his supervision of the project and for the valuable technical discussions.

The radiating element used in the measurements was developed and tested within the ESA-funded TDE activity ”Scalable and Deployable Active Phased Array Antenna for Future Satcom Payloads.” The authors thank Giovanni Toso for his supervision of this activity and for his insightful contributions throughout the project.

References

[1] J.-P. Fraysse and all, “Acta-uhts project – overview of challenges and enablers for the development of very large

dra for telecom satellites in ka band," in *41st ESA Antenna Workshop*, 2023.

[2] E. Girard, J.-P. Fraysse, and H. Legay, "Dual band, dual polarization shared aperture ka tx/rx phased array for ultra high throughput satellite," in *2025 19th Eur. Conf. on Antennas and Prop. (EuCAP)*, 2025.

[3] K. K. Chan and S. K. Rao, "Design of high efficiency circular horn feeds for multibeam reflector applications," *IEEE Trans. on Antennas and Prop.*, vol. 56, no. 1, pp. 253–258, 2008.

[4] J. D. Binion, C. A. Mussman, E. Lier, T. H. Hand, and D. H. Werner, "Dual-band advanced short backfire antenna with 100% aperture efficiency over a wide range of diameters," *IEEE Trans. on Antennas and Prop.*, vol. 70, no. 9, pp. 7786–7797, 2022.

[5] H. Zhao, P. F. Gu, Z. H. Fan, Z. He, J. Cao, X. Tao, J. X. Wang, and D. Z. Ding, "Ultrawideband dual circularly polarized waveguide array antenna for k- and ka-bands satellite communications," *IEEE Antennas and Wireless Prop. Lett.*, vol. 22, no. 8, pp. 1808–1812, 2023.

[6] S. M. A. Momeni Hasan Abadi and N. Behdad, "Wideband linear-to-circular polarization converters based on miniaturized-element frequency selective surfaces," *IEEE Trans. on Antennas and Prop.*, vol. 64, no. 2, pp. 525–534, 2016.

[7] L. Young, L. Robinson, and C. Hacking, "Meander-line polarizer," *IEEE Trans. on Antennas and Prop.*, vol. 21, no. 3, pp. 376–378, 1973.

[8] Y. Chen, G. Zhai, S. Wang, J. Gao, and J. Ren, "Dual-band single-layered linear-to-dual-circular polarization converter with high angle stability for satellite communication," *IEEE Antennas and Wireless Prop. Lett.*, vol. 22, no. 8, pp. 2017–2021, 2023.

[9] A. Ericsson and D. Sjöberg, "Design and analysis of a multilayer meander line circular polarization selective structure," *IEEE Trans. on Antennas and Prop.*, vol. 65, no. 8, pp. 4089–4101, 2017.

[10] F. A. Dicandia and S. Genovesi, "Linear-to-circular polarization transmission converter exploiting meandered metallic slots," *IEEE Antennas and Wireless Prop. Lett.*, vol. 21, no. 11, pp. 2191–2195, 2022.

[11] P. Naseri, S. A. Matos, J. R. Costa, C. A. Fernandes, and N. J. G. Fonseca, "Dual-band dual-linear-to-circular polarization converter in transmission mode application to k/ka -band satellite communications," *IEEE Trans. on Antennas and Prop.*, vol. 66, no. 12, pp. 7128–7137, 2018.

[12] H. B. Wang and Y. J. Cheng, "Single-layer dual-band linear-to-circular polarization converter with wide axial ratio bandwidth and different polarization modes," *IEEE Trans. on Antennas and Prop.*, vol. 67, no. 6, pp. 4296–4301, 2019.

[13] J. Lundgren, O. Zetterstrom, F. Mesa, N. J. G. Fonseca, and O. Quevedo-Teruel, "Fully metallic dual-band linear-to-circular polarizer for k/ka-band," *IEEE Antennas and Wireless Prop. Lett.*, vol. 20, no. 11, pp. 2191–2195, 2021.

[14] C. Molero, E. Menargues, and M. García-Vigueras, "All-metal 3-d frequency-selective surface with versatile dual-band polarization conversion," *IEEE Trans. on Antennas and Prop.*, vol. 68, no. 7, pp. 5431–5441, 2020.

[15] C. Molero, H. Legay, T. Pierré, and M. García-Vigueras, "Broadband 3d-printed polarizer based on metallic transverse electro-magnetic unit-cells," *IEEE Trans. on Antennas and Prop.*, vol. 70, no. 6, pp. 4632–4644, 2022.

[16] H. P. Chen, R. S. Hao, Y. Xia, Z. Li, X. Gu, and Y. J. Cheng, "K/ka-band shared-aperture all-metal polarizer based on ridge waveguide," *IEEE Antennas and Wireless Prop. Lett.*, pp. 1–5, 2025.

[17] A. Guarriello, G. Courtin, R. Loison, and R. Gillard, "A general equivalent circuit model for phoenix cells," *IEEE Trans. on Antennas and Prop.*, vol. 69, no. 11, pp. 7982–7986, 2021.

[18] C. Stoumpos, L. Polo-López, H. Legay, T. Pierré, and M. García-Vigueras, "Blazed 3-d cells with application to full-metal dichroic mirrors," *IEEE Trans. on Antennas and Prop.*, vol. 72, no. 11, pp. 8404–8419, 2024.

[19] D. Bermúdez-Martín, R. Gillard, C. Molero, H. Legay, and M. García-Vigueras, "Methodology for improving scanning performance loading an array element with a 3d all-metal waim," *Electronics*, vol. 11, no. 18, p. 2848, 2022.

[20] C. Stoumpos, J.-P. Fraysse, G. Goussetis, R. Sauleau, and H. Legay, "Quad-furcated profiled horn: The next generation highly efficient geo antenna in additive manufacturing," *IEEE Open Jour. of Antennas and Prop.*, vol. 3, pp. 69–82, 2022.